Chapter 2
Tether and Bridle Line Drag in Airborne Wind Energy Applications

Storm Dunker

Abstract This chapter discusses the physics of tether and bridle line drag based on literature, describes the typical flight regimes for airborne wind energy and identifies regimes of elevated drag caused by vortex-induced vibration and movement-induced excitation such as galloping. The presented laboratory tests show increases of aerodynamic drag due to vortex-induced vibration up to 300% and due to galloping up to 210%. Given that tether drag is a primary limitation to an airborne wind energy system's ability to fly faster and produce more energy, understanding the regimes of elevated drag as well as the mechanisms to suppress the causing phenomena are important. The chapter provides a basic overview of these phenomena as well as potential solutions for drag reduction. The information and material presented should provide an airborne wind energy developer a useful introduction to the considerations of tether and bridle line aerodynamic drag.

2.1 Introduction

As the name implies, airborne wind energy (AWE) is the conversion of wind energy by of one or more flying, buoyant or otherwise lifted devices into electrical energy. All conversion concepts employ one or more tethers to mechanically connect the lift devices to the ground. Many concepts use additional bridle lines to further distribute the load transfer from the lifting device to the tethers. AWE systems are either of the Ground-gen variant (generators located on the ground, operated by a tether wrapped around a coupled drum, the reeling out and in of the tether converting linear motion into shaft power) or of the Fly-gen variant (generators located on the lifting device are driven by impellers, the generated electrical power transmitted down a tether of fixed length). Ground-gen systems are, for example, developed by Enerkite and TU

Storm Dunker (✉)
A-Z Chuteworks LLC., Houston, TX, USA
e-mail: storm@azc-llc.com

R. Schmehl (ed.), *Airborne Wind Energy*, Green Energy
and Technology, https://doi.org/10.1007/978-981-10-1947-0_2

Delft, while Fly-gen systems are developed by Makani and Altaeros Energies. More comprehensive overviews of implemented concepts are presented in [7, 26].

Tethers and bridle lines are textile components forming a tensile structure that is designed and optimized for the transfer of tensile loads but unsuitable for supporting compression loads. Bridle lines cascade out of the tether, are thinner than tethers due to distributed load, generally have a shorter length and connect to the lifting device in several attachment points. Tethers for Fly-gen systems are generally thicker and heavier because they incorporate additional conductive wires to transmit electric energy. These wires can be contained inside the core of a braided tether or can be braided among the other braiding carriers as part of the braid itself.

Loyd [20] derived analytical models for the achievable power output from simple kites that perform only a reel out motion and kites that are additionally flown in crosswind maneuvers. A key parameter in these models is the aerodynamic lift-to-drag ratio L/D of the kite. Power output in Loyd's crosswind model, in which systems principally operate at relative airspeeds up to L/D times higher than for simple, non-maneuvering kites, is especially sensitive to the aerodynamic drag contributions of tethers and bridle lines. In particular the drag of long tethers can represent a significant part of total drag of crosswind kites. Reduced tether drag directly increases L/D which according to Loyd's theory increases the flight velocity, the tether tension and consequently also the power output.

The aerodynamic properties of tethers and bridle lines depend on the local relative flow conditions, which, for a static setup includes the orientation with respect to the relative flow, the flow cross section and the surface characteristics of the exposed material. However, as a result of its inherent elasticity and inertia, the tensile structure can be exited by the relative flow to oscillate. Aero-structural coupling phenomena such as Vortex-Induced Vibrations (VIV) and galloping can increase drag significantly and cause other unwanted dynamic effects.

This chapter is structured as follows. Section 2.2 presents a mathematical framework for the description of tensioned tethers and bridle lines in a cross flow environment and discusses various assumptions to simplify the physical problem. Section 2.3 discusses the operating envelopes assumed for all AWE applications that could use tethers and bridle lines. Section 2.4 will then review basic background physics, specifically from early chapters of Blevins' Flow-Induced Vibrations [3], relevant to the domain of aerodynamic drag for tethers and bridle lines. Related VIV and galloping experiments of bridle lines, either from the author or from literature, are presented in Sect. 2.5. Finally, in Sect. 2.6, potential tether design solutions are introduced that could help control elevated drag regimes.

2.2 Mathematical Framework and Assumptions

Throughout this chapter, the following descriptions and assumptions apply unless stated otherwise. The tether and the bridle lines are evaluated as an elastic flexible structure that can stretch, twist and dynamically oscillate along and perpendicular to

the relative flow. The movement of this structure in the wind field is described in the wind reference frame x_w, y_w, z_w, which has its origin **O** located at the ground attachment point of the tether. The x_w-axis of this reference frame is aligned with the wind velocity $\mathbf{v}_w$, which is assumed to be constant in time and uniform in space, while its z_w-axis is pointing upward. The tether is assumed to be straight and accordingly the radial coordinate r can be used to describe positions on the tether

$$\mathbf{r} = r\,\mathbf{e}_r. \tag{2.1}$$

This configuration is illustrated in Fig. 2.1. The value of the radial coordinate varies between 0 at the origin and the tether length l_t at the kite **K**. A corresponding non-dimensional tether coordinate can be defined as

$$R = \frac{r}{l_t}. \tag{2.2}$$

The tether length is generally not constant but varies as a result of the reeling motion and to a minor degree also the strain of the tether. It is important to note that the radial coordinate r is a geometric measure which does not describe material points on the tether. Because of the reeling motion, the radial velocity $\mathbf{v}_{t,r}$ of material points is constant along the tether when neglecting strain, and equal to the radial velocity $\mathbf{v}_{k,r}$ of the kite

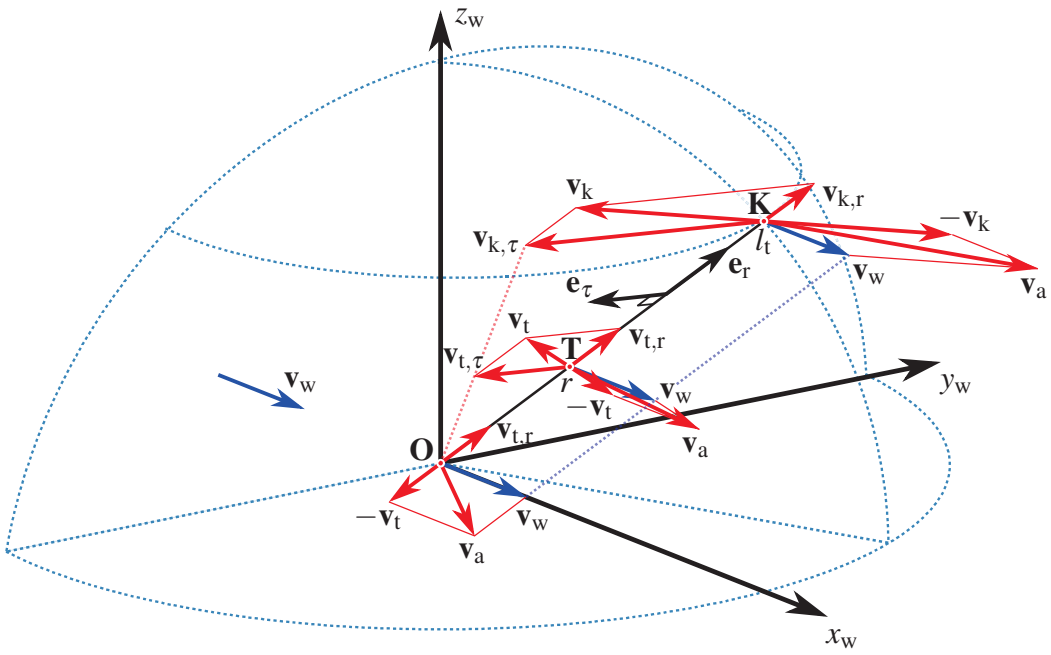

Fig. 2.1 Relative flow conditions at the origin **O**, an arbitrary point **T** along the tether and the kite **K**. A point on the tether moves with the material velocity $\mathbf{v}_t$, consisting of radial and tangential components $\mathbf{v}_{t,r}$ and $\mathbf{v}_{t,\tau}$, respectively. The tip of the tether at $r = l_t$ moves with the kite velocity, i.e. $\mathbf{v}_t = \mathbf{v}_k$. The radial unit vector $\mathbf{e}_r = \mathbf{v}_{k,r}/v_{k,r}$ is aligned with the tether, while the tangential unit vector $\mathbf{e}_\tau = \mathbf{v}_{k,\tau}/v_{k,\tau}$ is perpendicular and pointing in the flight direction of the kite

$$\mathbf{v}_{t,r} = \mathbf{v}_{k,r}, \qquad \text{for} \quad 0 \le R \le 1. \tag{2.3}$$

The tangential velocity $\mathbf{v}_{t,\tau}$ is constrained to zero at the ground attachment point **O** and is identical to the tangential velocity $\mathbf{v}_{k,\tau}$ of the kite at the kite attachment point **K**. It can be formulated as a linear function of the radial coordinate

$$\mathbf{v}_{t,\tau} = \mathbf{v}_{k,\tau} R, \qquad \text{for} \quad 0 \le R \le 1. \tag{2.4}$$

The material velocity $\mathbf{v}_t = \mathbf{v}_{t,r} + \mathbf{v}_{t,\tau}$ of a point on the tether can thus be related to the radial and tangential velocity components of the kite by

$$\mathbf{v}_t = \mathbf{v}_{k,r} + \mathbf{v}_{k,\tau} R, \qquad \text{for} \quad 0 \le R \le 1. \tag{2.5}$$

The apparent wind velocity of a material point on the tether is defined as

$$\mathbf{v}_a = \mathbf{v}_w - \mathbf{v}_t, \tag{2.6}$$

$$= \mathbf{v}_w - \mathbf{v}_{k,r} - \mathbf{v}_{k,\tau} R, \qquad \text{for} \quad 0 \le R \le 1, \tag{2.7}$$

which is visualized in Fig. 2.1 for an arbitrary point **T** along the tether and for the end points **O** and **K**, respectively. From Eq. (2.7) and Fig. 2.1 it is obvious that the apparent wind velocity along the moving tether varies in magnitude and direction.

The relative flow conditions are further detailed in Fig. 2.2. The angle of attack

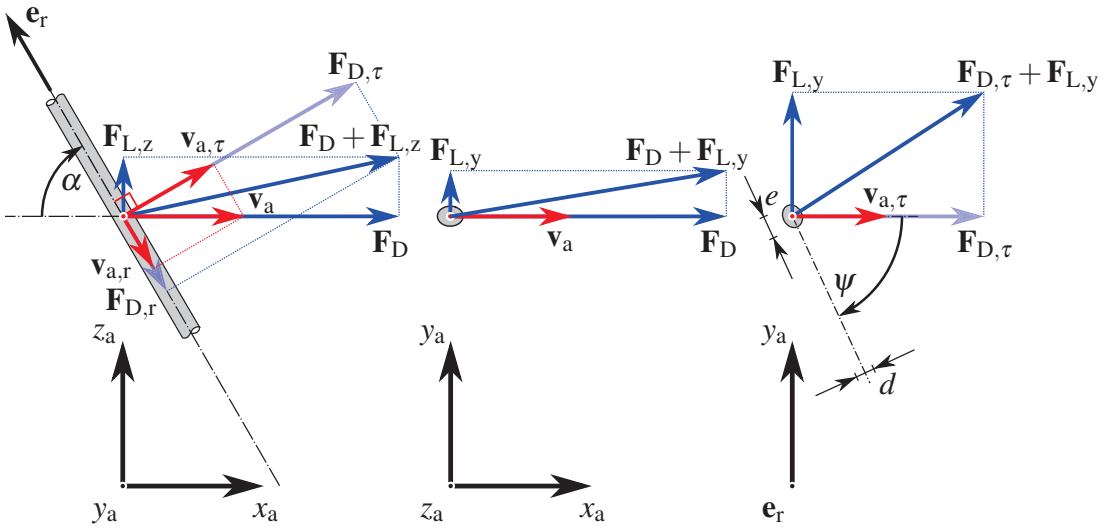

(a) Side view of a cylindrical tether segment, inclined towards the relative flow

(b) Top view of a cylindrical tether segment, inclined towards the relative flow

(c) Axial view of a twisted tether with deformed elliptical cross section

Fig. 2.2 (a) Definition of the local angle of attack α of a cylindrical tether segment, relative flow velocity $\mathbf{v}_a = \mathbf{v}_{a,\tau} + \mathbf{v}_{a,r}$ and total aerodynamic force $\mathbf{F}_a = \mathbf{F}_D + \mathbf{F}_{L,y} + \mathbf{F}_{L,z} = \mathbf{F}_{D,\tau} + \mathbf{F}_{L,y} + \mathbf{F}_{D,r}$ in a side view, (b) same configuration in top view with the resulting elliptical cylinder section, (c) definition of the local angle of incidence ψ of a twisted tether with deformed elliptical cross section in an axial view. The relative flow reference frame x_a, y_a, z_a is constructed from the local apparent wind velocity vector $\mathbf{v}_a$ and the radial unit vector $\mathbf{e}_r$. By definition $\mathbf{F}_{D,\tau}$ is aligned with $\mathbf{v}_{a,\tau}$

α of the tether or bridle line segment is measured from the local apparent wind velocity $\mathbf{v}_\mathrm{a}$ to the tether axis, which coincides with the radial unit vector $\mathbf{e}_\mathrm{r}$, and relates the radial and tangential velocity components to the magnitude as follows

$$v_{\mathrm{a,r}} = v_\mathrm{a} \cos\alpha \tag{2.8}$$

$$v_{\mathrm{a},\tau} = v_\mathrm{a} \sin\alpha. \tag{2.9}$$

The radial and tangential components of the apparent wind velocity are defined as

$$\mathbf{v}_{\mathrm{a,r}} = (\mathbf{v}_\mathrm{a} \cdot \mathbf{e}_\mathrm{r})\,\mathbf{e}_\mathrm{r}, \tag{2.10}$$

$$\mathbf{v}_{\mathrm{a},\tau} = \mathbf{v}_\mathrm{a} - \mathbf{v}_{\mathrm{a,r}}, \tag{2.11}$$

while the magnitudes of these components can be calculated from Eq. (2.7) as functions of the corresponding wind and kite velocity components

$$v_{\mathrm{a,r}} = v_{\mathrm{w,r}} - v_{\mathrm{k,r}}, \tag{2.12}$$

$$v_{\mathrm{a},\tau} = v_{\mathrm{w},\tau} - v_{\mathrm{k},\tau} R. \tag{2.13}$$

As illustrated in Fig. 2.2 the aerodynamic force $\mathbf{F}_\mathrm{a}$ acting on the tether segment can be represented in the relative flow reference frame $x_\mathrm{a}, y_\mathrm{a}, z_\mathrm{a}$ by a drag component $\mathbf{F}_\mathrm{D}$ and two perpendicular lift components $\mathbf{F}_{\mathrm{L,y}}$ and $\mathbf{F}_{\mathrm{L,z}}$. The lift component $\mathbf{F}_{\mathrm{L,z}}$ is caused by the inclination of the cylinder, while the lift component $\mathbf{F}_{\mathrm{L,y}}$ is generally fluctuating as a result of unsteady flow separation from the cylinder. Alternatively, the aerodynamic force can be decomposed into a tangential drag force $\mathbf{F}_{\mathrm{D},\tau}$ acting perpendicularly to the tether and in line with $\mathbf{v}_{\mathrm{a},\tau}$, an axial drag force $\mathbf{F}_{\mathrm{D,r}}$ acting in line with the tether and a transverse lift force $\mathbf{F}_{\mathrm{L,y}}$ acting perpendicularly to the tether and to $\mathbf{v}_{\mathrm{a},\tau}$. This alternative representation will be used in Sect. 2.4.1 to theoretically construct the aerodynamic loading of a tether segment that is inclined with respect to the relative flow.

As a first approximation a tether or line segment can be represented by a circular cylinder. However, there are many practical situations where such approximation is not appropriate. For example, when tapes are used as part of the bridle line system [34] or when the originally cylindrical line is twisted under tension such that the cross section deforms significantly. To characterize deviations from the circular cross section the ellipse ratio e/d is introduced. The definition of the twist angle ψ of a tether with deformed elliptical cross section is shown in Fig. 2.2(c). Because this angle characterizes the orientation of the cross section with respect to the normal component of the relative flow, it can also be regarded as incidence angle. The inclination of the elliptical shape leads to a steady transverse lift component $\mathbf{F}_{\mathrm{L,y}}$. A tether with circular cross section is characterized by $e/d = 1$, which, for simplicity, is the assumed shape unless stated otherwise. While yaw of the flying device will add twist to the tether, this chapter assumes no yaw of the flying device.

It is also assumed, unless due to VIV or plunge galloping defined later, that the nominal orientation of the tether section parameter d is perpendicular to the relative flow, as shown in Figs. 2.2(c). Reference test data is often only available for rigid

circular cylinders. The angle of twist ψ varies along the tether and by that also the local lift and drag contributions. Depending on the torsional stiffness of the tether, the relative flow can induce an aero-structural coupling phenomenon which is denoted as torsional galloping.

A tether or line is also able to vibrate with a transverse motion such as seen during VIV and a phenomenon denoted as plunge galloping. The vibrations typically have a high frequency and a time scale that is much shorter than the flight dynamic time scale of the kite. The kinematics and the mechanism of the aero-elastic phenomenon are illustrated in Fig. 2.3. The amplitude of the vibration is A_y, the transverse velocity of the tether or line experiencing transverse vibration is $v_{t,\omega}$ and the resulting vibration-induced angle of attack is α_ω. Both $v_{t,\omega}$ and α_ω vary with time and are often assumed to follow a sine curve for steady vibrations. The transverse velocity $v_{t,\omega}$ requires the modification of the apparent wind velocity from v_a to the vibration-induced relative flow velocity

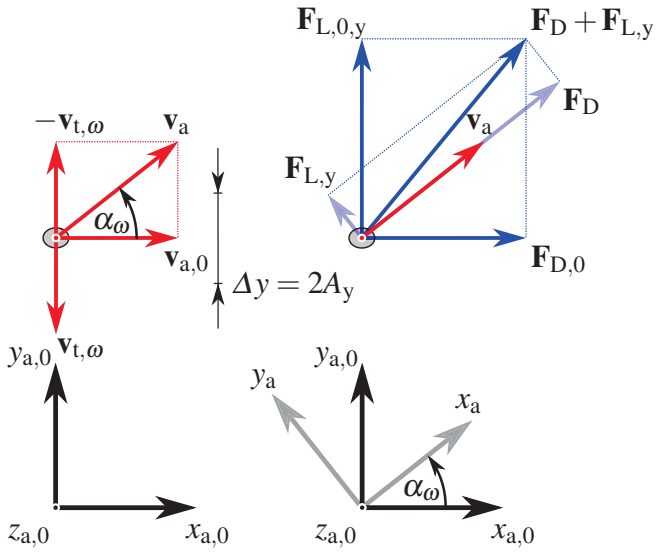

Fig. 2.3 Transverse oscillation of the tether with velocity $\mathbf{v}_{t,\omega}$ and resulting vibration-induced angle of attack α_ω (left), decomposition of the resulting aerodynamic force $\mathbf{F}_a$ into drag and lift components $\mathbf{F}_D$, $\mathbf{F}_{L,y}$ and $\mathbf{F}_{L,z}$ which can be transformed back into force components $\mathbf{F}_{D,0}$, $\mathbf{F}_{L,0,y}$ and $\mathbf{F}_{L,0,z}$ in the mean relative flow reference frame $x_{a,0}, y_{a,0}, z_{a,0}$ (right)

$$v_a = \sqrt{v_{a,0}^2 + v_{t,\omega}^2}, \tag{2.14}$$

where $v_{a,0}$ is the mean relative flow velocity. Since the transverse vibration mode is possible without twist of the tether or line, the flow-induced transverse vibrations can lead to a significant increase of aerodynamic lift and drag.

Throughout the chapter, the tethers and bridle lines are evaluated as discrete components rather than with system-level interactions. This chapter does not attempt to cover impacts of system-level dynamics, such as other than aerodynamic influences, e.g. wave transmission along the tether from the flying vehicle, varying tension forcing functions from the flying vehicle, elastic behavior of a textile tether, inertial resistance to vehicle motion, etc.

2.3 Operating Envelope for Airborne Wind Energy Applications

Prior to discussing the applicable physics of tethers and bridle lines in a cross flow environment, the ranges of potential operating and environmental conditions are defined. The variables involved are the apparent wind velocity, air density, temperature, tether diameters, tether angles of attack and derived nondimensional parameters such as Reynolds number.

For the purposes of the study, all of the pursued AWE concepts are considered and a set of generic ranges of these parameters is proposed. The considerations include systems that operate at low altitudes and not yet access high altitudes, static and dynamic AWE systems with tethers that are still or move, Ground-gen and Fly-gen systems, ranges of tether or line diameter and temperature ranges based on geography and operating altitude.

A simplified range of airspeeds would be from a low speed of 2.5 $\mathrm{m/s}$ low (static tether AWE system) up to a high speed of 80 $\mathrm{m/s}$ high (dynamic tether AWE system) [12]. The air density could theoretically range from below sea level, say 1.235 $\mathrm{kg/m^3}$ standard day, towards the upper region of the conceived operating area, basically the jet stream or approximately 0.253 $\mathrm{kg/m^3}$, which is not yet accessible due to existing airspace restrictions and possible technical challenges. Temperatures could range from -60° C at upper altitudes to $+45^\circ$ C in lower deserts. It is noted that the minimum temperature occurs at maximum altitude and vice versa.

Tether and line diameters scale with the power output of the AWE systems because the tensile force is the primary dependency. The anticipated range of diameters covering the smallest lines to the largest tethers is assumed to be 1 to 50 mm.

Assuming steady and uniform wind, a maximum tether angle of attack could theoretically be at or near 90° for a portion of a tether when a system overflies the wind window. This could occur due to reel in of the tether and due to the wing's inertia when on a flight trajectory with a continuously increasing inclination angle. Most lines used in bridling have individual angles of attack different from the tether (and each other) where some of these could very likely encounter a 90° angle of attack. A minimum tether angle of attack could also be very low, depending on non-nominal wind conditions and landing maneuvers. For the purpose of this study, a range from 0 to 90° is considered possible for AWE tethers and bridle lines.

2.4 Physics of Tensioned Cables in Cross Flows

Tethers and bridle lines are essential for the load transfer from the airborne lifting device to the ground. The movement of this tensile structure in a wind field creates an additional aerodynamic loading. While the fluid-dynamic pressure on the leading edge of the cylindrical components is higher than in free stream, the pressure on the sides and trailing edge is lower. The integral pressure and shear stress results in an aerodynamic force on the tensile structure. The trailing wake flow is often turbulent and organized by discrete swirling vortices that shed from the sides of

the structure in an alternating phase. The resulting aerodynamic forces are unsteady and can interact with the structure producing movement or deformation, leading to a coupling of fluid and structural motion (fluid-structure interaction). This section details the relevant physical processes.

2.4.1 Aerodynamic Forces and Flow Regimes

As outlined in Sect. 2.2, the aerodynamic force on a cylindrical structure can be decomposed into a drag component, acting in x_a-direction which is aligned with the relative flow, and lift components, acting in y_a- and z_a-directions which are perpendicular to the relative flow. The alternating vortex shedding produces a cyclic loading which can initiate or propagate vibrations of the tensile structure. The vibrations are substantially amplified if the frequency of vortex shedding, i.e. the period of the load cycles, is near a specific harmonic resonance of the structure, at its natural frequency.

According to Hoerner [15] and Bootle [4] the aerodynamic force acting on an inclined circular cylinder in a low-speed flow can be approximated as a superposition of a normal drag contribution $F_{\mathrm{D},\tau}$, depending on the normal velocity component $v_{\mathrm{a},\tau}$, and an axial drag contribution $F_{\mathrm{D,r}}$, depending on the axial velocity component $v_{\mathrm{a,r}}$. The essence of this "cross flow principle" is that the two perpendicular drag components illustrated in Fig. 2.2(a) are evaluated independently

$$F_{\mathrm{D},\tau} = \frac{1}{2}\rho C_{\mathrm{D},\tau} l_\mathrm{t} d v_{\mathrm{a},\tau}^2, \tag{2.15}$$

$$F_{\mathrm{D,r}} = \frac{1}{2}\rho C_\mathrm{f} l_\mathrm{t} \pi d v_{\mathrm{a,r}}^2, \tag{2.16}$$

where $C_{\mathrm{D},\tau}$ is the drag coefficient of a cylinder at $\alpha = 90°$, C_f is the skin friction drag coefficient, $l_\mathrm{t} d$ is the flow cross section of a cylinder segment, $l_\mathrm{t}\pi d$ is the wetted surface area of the segment and ρ is the fluid density.

The two force components can be transformed back to the mean relative flow reference frame and, using Eqs. (2.8) and (2.9), expressed as functions of the relative flow velocity v_a

$$F_\mathrm{D} = \frac{1}{2}\rho \left(C_{\mathrm{D},\tau}\sin^3\alpha + C_\mathrm{f}\pi\cos^3\alpha\right) l_\mathrm{t} d v_\mathrm{a}^2, \tag{2.17}$$

$$F_{\mathrm{L,z}} = \frac{1}{2}\rho \left(C_{\mathrm{D},\tau}\sin^2\alpha\cos\alpha - C_\mathrm{f}\pi\cos^2\alpha\sin\alpha\right) l_\mathrm{t} d v_\mathrm{a}^2, \tag{2.18}$$

which leads to the following aerodynamic drag and lift coefficients [4]

$$C_\mathrm{D} = C_{\mathrm{D},\tau}\sin^3\alpha + C_\mathrm{f}\pi\cos^3\alpha, \tag{2.19}$$

$$C_{\mathrm{L,z}} = C_{\mathrm{D},\tau}\sin^2\alpha\cos\alpha - C_\mathrm{f}\pi\cos^2\alpha\sin\alpha. \tag{2.20}$$

In extension of the "crosswind principle", the transverse aerodynamic lift force acting in y_a-direction on a cylinder with arbitrary cross section can be represented as

$$F_{L,y} = \frac{1}{2}\rho C_{L,\tau} l_t d v_{a,\tau}^2, \tag{2.21}$$

where $C_{L,\tau}$ is the lift coefficient at $\alpha = 90°$. This leads to the following transverse lift coefficient

$$C_{L,y} = C_{L,\tau} \sin^2 \alpha. \tag{2.22}$$

In summary, it can be stated that the coefficients defined by Eqs. (2.19), (2.20) and (2.22) are multiplied by the square of the relative flow velocity v_a and a term $1/2\,\rho l_t d$ to determine the drag and lift force components F_D, $F_{L,z}$ and $F_{L,y}$ acting on the inclined cylinder segment.

The aerodynamic forces generated by a transverse oscillation of the cylinder are illustrated in Fig. 2.3. The vibration-induced force components F_D and $F_{L,y}$ can be transformed into the mean flow reference frame as follows

$$F_{D,0} = F_D \cos \alpha_\omega - F_{L,y} \sin \alpha_\omega, \tag{2.23}$$

$$F_{L,0,y} = F_D \sin \alpha_\omega + F_{L,y} \cos \alpha_\omega. \tag{2.24}$$

To account for the varying relative flow conditions along the moving tether, higher order models generally discretize the tether into connected segments [6]. The aerodynamic forces are evaluated per segment, based on the local apparent wind velocity v_a and angle of attack α, and the equations of motion are solved by stepwise integration over the tether elements.

For the subsonic flows that are relevant within the scope of the chapter, the aerodynamic coefficients depend primarily on the Reynolds number

$$\mathrm{Re} = \frac{v_a d}{\nu}, \tag{2.25}$$

where ν is the dynamic viscosity of the air. In essence, the non-dimensional number is a measure for the ratio of inertial forces and viscous forces in the fluid flow around the cable.

Considering the ranges of apparent wind velocity, tether diameter and kinematic viscosity of air discussed in Sect. 2.3, the expected range of the Reynolds number for AWE applications in general is $42 < \mathrm{Re} < 2.9 \times 10^5$. A specific AWE application will have a much narrower range than this. With the exception of the thickest diameter tether, the majority of tethers and bridle lines operate below the critical Reynolds number condition of $\mathrm{Re}_{crit} \approx 3.5 \times 10^5$ within the sub-critical range defined as $300 < \mathrm{Re} < 1.5 \times 10^5$ [3].

Using the stated operating regimes, the cross flow drag coefficient and the axial skin friction drag coefficient can be plotted as functions of the Reynolds number and together against the tether or line diameter. The result is illustrated in Fig. 2.4. The plotted data for the drag coefficient is time-averaged and does not resolve the fluctuations caused by the unsteady flow separation from the cylinder. The data is

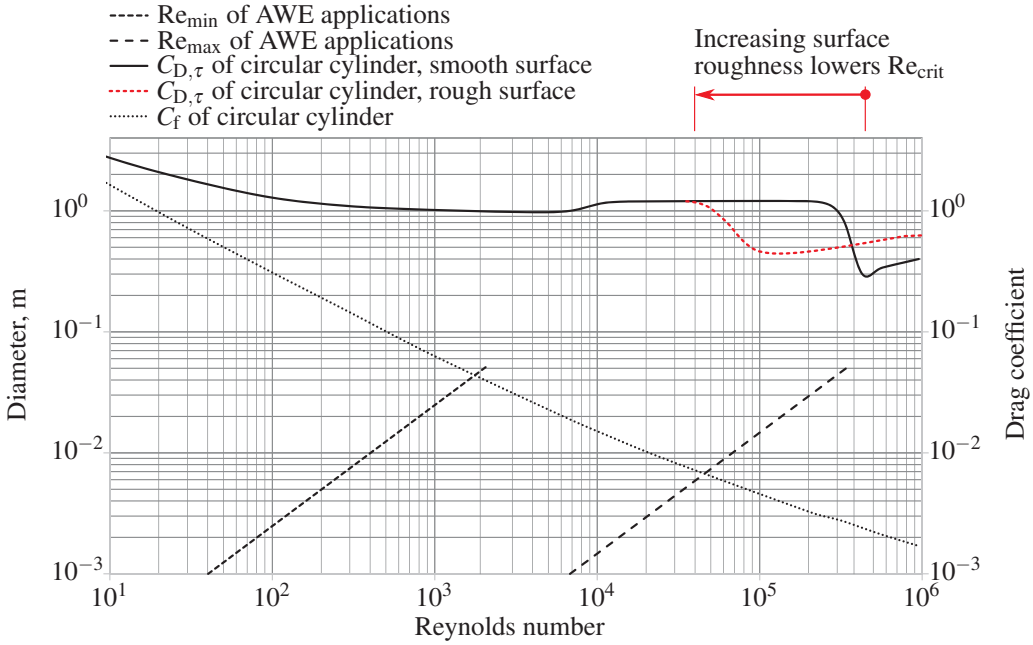

Fig. 2.4 Minimum and maximum Reynolds numbers $\mathrm{Re}_{\min}$ and $\mathrm{Re}_{\max}$, respectively, as functions of cylinder diameter d, mean cross flow drag coefficients $C_{\mathrm{D},\tau}$ of circular cylinders with smooth and rough surface and skin friction drag coefficient C_{f} of a circular cylinder in axial flow [15, 25]

sourced from circular cylinders which can be assumed to be smooth and have low surface roughness when compared to braided AWE tethers and bridle lines. The critical Reynolds number trends toward lower values and shallower dips with increasing roughness [11, 15, 25]. For cylinders with a rough surface, the critical Reynolds number region can be as low as 3.0×10^4, which is within the range of the top end Reynolds numbers for larger diameter tethers. However, the reduction of drag at the critical Reynolds number diminishes as surface roughness increases. The roughness performance data is based on tests using sand grains of a specific size adhered to a cylinder surface, with surface roughness being between 0.005 to 0.02 (sand grain size to cylinder diameter). In the reference data, drag reduction at the critical Reynolds number appears to trend towards no or negligible drag reduction at a Reynolds number of about 3×10^4 for surface roughness greater than 0.02.

From Fig. 2.4, the approximate range of aerodynamic drag coefficients for a cylinder with $\alpha = 90^\circ$ in the AWE Reynolds number range of interest is $0.98 < C_{\mathrm{D}} < 1.8$. The skin friction coefficients vary to a much greater extent. The skin friction coefficient values are less than 10% of the drag coefficient for Reynolds numbers above about 500. While the friction coefficient is much lower than the aerodynamic drag coefficient, it should be noted that the wetted area is at least π times the section area used for aerodynamic drag calculation, depending on angle of attack, which increases the relative importance of skin friction.

2.4.2 Unsteady Vortex Shedding

The principles of unsteady vortex formation from a circular cylinder are well documented by Blevins [3]. The relevant flow phenomenon for AWE applications is that of a fully turbulent vortex street, occurring in the range from $300 < \mathrm{Re} < 2.9 \times 10^5$ and illustrated in Fig. 2.5.

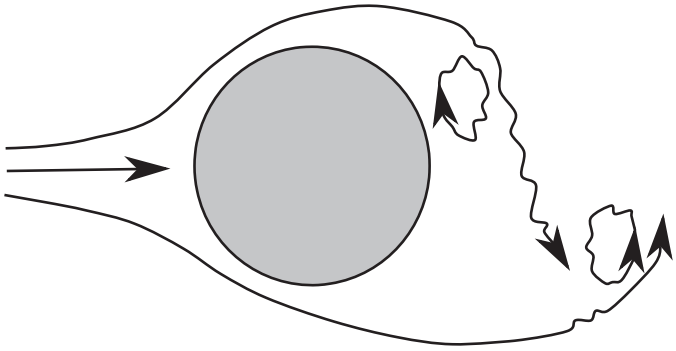

Fig. 2.5 Illustration of a fully turbulent vortex street relevant for AWE applications [19]

When evaluating in two dimensions, the vortex shedding from a rigid stationary cylinder generates a resultant force vector that oscillates in magnitude and direction, as shown in Fig. 2.6. In reference to Drescher [8], the direction of the resultant force vector, which is composed of lift and drag components, varies between $-45°$ and $45°$ at $\mathrm{Re} = 1.12 \times 10^5$. The pressure oscillation occurs at a specific frequency and can be described in terms of the Strouhal number. This non-dimensional number is defined as

$$\mathrm{St} = \frac{f_\mathrm{s} d}{v_\mathrm{a}} \tag{2.26}$$

and used to characterize oscillating flow mechanisms. It relates the shedding frequency f_s to the freestream velocity v_a and the characteristic length d of a subject

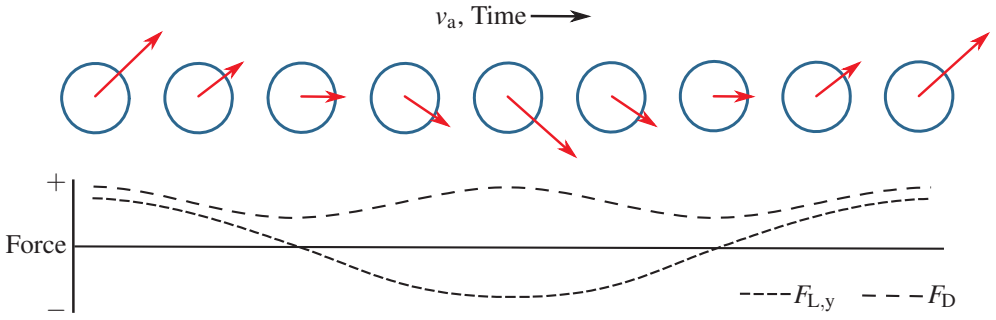

Fig. 2.6 Generic resultant pressure vector for one complete vortex shedding cycle compared against chronologically aligned plot of notional flow-aligned and -transverse force components

body or diameter for tethers and bridle lines. By inverting Eq. (2.26) the shedding frequency can be represented as a function of the Strouhal number.

An approximation of various Strouhal numbers for rough and smooth surfaces, taken from [3], is shown in Fig. 2.7 and combined with observations of Strouhal numbers from AWE relevant testing of kitesurfing line from Dunker [9].

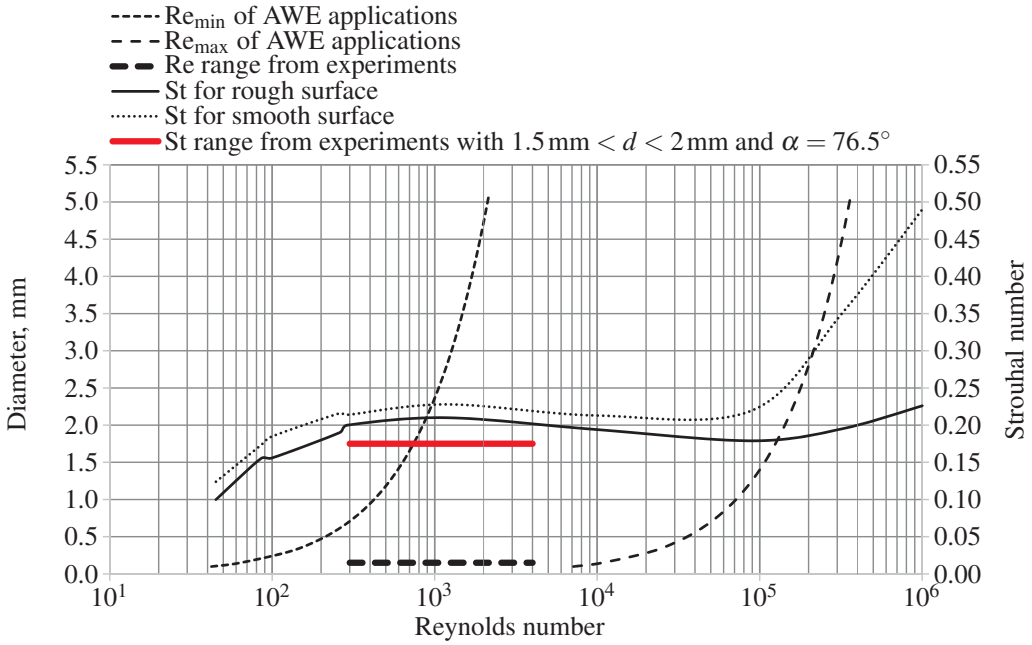

Fig. 2.7 Minimum and maximum Reynolds number of AWE applications as functions of tether diameter, Reynolds number range from experiments, Strouhal number as function of Reynolds number from literature sources for circular cylinders at $\alpha = 90°$ and from experiments with bridle lines at $\alpha = 76.5°$

Given the structural composition and design of a braided tether or bridle line, its surface can be assumed to be rough. Excluding Reynolds numbers below about 300, the Strouhal number for AWE applications is about 0.20. This corresponds to one vortex shedding cycle for every 5 body diameters of airflow past the tether, bridle line or cylinder. The performed tests with braided lines of diameters ranging from 15 to 20 mm, showed Strouhal numbers ranging from 0.17 to 0.18 [9]. The tests were performed with $\alpha = 76.5°$, which according to Eq. (2.17) results in a 10% decrease of drag.

In his original research, Strouhal noted that audible tones resulting from flow around a cylinder were not a function of tension or cylinder length, which in essence means that the natural frequency did not affect the production of the Strouhal frequency tones [30]. Rather, an increase in length of a cylinder produced a louder tone of the same frequency.

2.4.3 Effect of Inclination

An inclination of the cylinder with respect to the relative flow has a predictable effect on shedding frequencies for small deviations from the perpendicular orientation (indicated by subscript n). King [18] proposed a correlation

$$f_s = f_{s,\tau} \sin \alpha, \qquad \text{for} \quad \alpha > 60^\circ, \tag{2.27}$$

where $f_{s,\tau}$ is the value for $\alpha = 90^\circ$.

Naudascher [21] reported that the prediction of vibration frequencies is more complicated for $\alpha < 60$. The shedding phenomenon becomes increasingly three-dimensional and there can be a drastic decrease in vortex strength. Shedding frequencies can also depend on the design of the cylinder tips. The lift force component, which is perpendicular to the relative flow, oscillates at the shedding frequency, but the drag force component, aligned with the flow, oscillates at twice the shedding frequency. This difference in oscillation frequencies is seen in Fig. 2.6. Seemingly, the lift force oscillations would reduce as vortex strength decreases.

Dunker recorded the dominant vibration frequency on several occasions at two times the shedding frequency, where the Reynolds number was close to 300, for $\alpha = 76.5^\circ$. Several secondary non-dominant frequencies were observed at two times the shedding frequency for Reynolds numbers up to about 1000.

2.4.4 Natural Frequency of the Tensile Structure

The free vibration characteristics of the tensile structure also determine how the structure responds to the fluctuating aerodynamic loading caused by unsteady vortex shedding. The effect on the aerodynamic drag can be substantial, for example, a string vibrating at its natural frequency can experience a higher than 300% increase compared to a non-vibrating string.

The natural frequencies f_n of an elastic string are the integer multiples of the fundamental frequency and can be formulated as

$$f_n = \frac{n}{2l_t}\sqrt{\frac{F_t}{\lambda}}, \qquad n = 1, 2, 3, \ldots, \tag{2.28}$$

where n is the vibration node number, l_t the length of string, F_t the tensile force and λ the mass per unit length, which is also denoted as linear density.

A common assumption for a vibrating string is that both ends of the string are fixed. For AWE applications the situation is different. The upper end of the tether is attached to a flying device which moves in space and exerts a traction force on the tether. However, compared to the tether the flying device has enough mass to consider it for the vibration dynamics as an end point with prescribed motion. The lower end of the tether is generally reeled from a winch at a fixed position. Many of

the implemented AWE systems use the winch control algorithm to constantly adjust the reeling speed to maintain the tether force below a permitted maximum value. It is clear that this particular setup and the effect on the vibration dynamics requires further investigation.

To assess the range of natural frequencies relevant for AWE applications and to compare with related applications, the lengths and tensions occurring during nominal flight conditions were estimated. To eliminate variations due to different cable materials Dyneema® SK75, was chosen as the primary tether material, with approximately $\lambda = 6.5 \times 10^{-6}$ kg/m per unit strength $F_t = 9.81$N provided. The particular material is a common selection for AWE and related industries due to its superior strength to weight and size properties. Various types of Dyneema material and the competing Spectra® material exist, both based on High Molecular Weight Polyethylene High Modulus Polyethylene (HMPE). Additional information about HMPE tethers is presented in Bosman [5].

Some AWE applications are based on ram-air wings or leading edge inflatable tube kites, which are also used for skydiving, paragliding and kite boarding [10]. The comparison of natural frequencies also includes these applications, using the strength of bridle lines of common commercial products. To setup a generalized comparison matrix, the bridle lines used for skydiving are rated at 2256 N (230 kgf), the lines for paragliding at 1128 N (115 kgf) and the lines for kite boarding at 2256 N (230 kgf). Multiplying these force ratings by $6.5/9.81 \times 10^{-6}$ kg/(Nm) yields the mass per unit length λ for each case. The strength of the AWE tether was selected to provide a minimum of 4 times the tension occurring in crosswind flight operation, based on commercially available materials. Natural frequencies occurring in AWE and related application areas are compared in Table 2.1.

Length of tether or bridle line, m

Line tension, N	1	7	8	10	15	30	50	400	>400
5	40.9	5.8	5.1	4.1					
15	70.9	10.1	8.9	7.1	3.3	1.7			
20	57.9	8.3	7.2	5.8	3.9	1.9			
70	108.9	15.5	13.5	10.8	7.2	3.6			
500					19.3	9.7	8.2	1.0	<1.0
5000							6.5	0.8	<0.8
50000							7.2	0.9	<0.9

		λ, kg/m
---------- Parachute bridling (skydiving)		0.00149
-------- Parachute and paraglider bridling		0.00075
———— Paraglider bridling		0.00149
-·-·-·- Kite boarding tether		0.00149
——— AWE tether	500 N	0.00075
	5000 N	0.01193
	50000 N	0.09542

Table 2.1 Comparison of natural frequencies occurring in AWE and related application areas

The lengths of tethers or bridle lines are based on personnel-sized commercially available products for the various industries listed. Generally speaking, ram-air skydiving parachutes and paragliders have the shortest bridle lines (upper cascading of suspension lines). The lines below the cascades are much longer, more so on paragliders than skydiving parachutes, which represent the top end of the limits. For kite boarding a short cascaded bridling up at the kite is used with much longer lines below the cascades down to the kite boarder. An arbitrary minimum length of 50 m is used for AWE applications.

The line tensions used for skydiving, paragliding and kite boarding are based on average human weights (plus assumptions for relevant equipment) distributed into the common tethering or bridling structure of the wings for that industry. This takes into account the number of lines used, cascading of lines and generic distribution of load among the lines. For AWE applications, generic line tensions were used. Values for line lengths and tensions were rounded.

2.4.5 Mass Ratio, Damping Factor and Mass Damping

An important indicator for the susceptibility of a tether or line to vortex-induced vibration is the mass ratio

$$m^* = \frac{\lambda}{\rho d^2}, \tag{2.29}$$

where λ is the tether mass per unit length and ρd^2 is proportional to the displaced fluid mass per unit length. The tether mass generally includes an added mass term representing a contribution of the fluid. Because of the large density ratio this term can be considered negligible.

The mass ratio relates two primary driving factors for vibrations of a cylinder in a transverse fluid flow. The cylinder mass in the numerator is a measure for the acceleration that the cylinder experiences in response to an external force. The fluid mass in the denominator, on the other hand, is a measure for the force that the fluid flow exerts on the cylinder. A higher cylinder mass or a lower fluid density result in a higher mass ratio and decrease the susceptibility to VIV. Conversely, a lower mass or higher density lead to a lower mass ratio and increase the susceptibility to VIV. It is inferred therefore that lower mass ratios, being more susceptible to VIV, are also associated with higher vibration amplitudes. Empirical data from Dale, Feng and Scruton described in [3] support this conclusion.

Therefore, tether or bridle lines made of fabric materials are likely more susceptible to VIV than heavier materials, such as wire or cable alternatives. This has a generally negative effect on AWE, since the tethers are desired to be as light as possible to minimize the airborne mass. The AWE industry has currently converged on Dyneema® and equivalent Spectra® materials with a density of around 0.97 g/cm^3. In laboratory tests, Dyneema lines with mass ratios of about $m^* = 720$ have exhibited strong VIV effects with corresponding significant increases in drag [9].

Slightly larger mass ratios can be expected from recent improvements in braiding efficiency or even from using tethers with sheaths and unbraided parallel fiber cores.

It should be noted that increasing the strength and diameter of a tether does not significantly change the mass ratio. As tethers are made stronger by including more fiber content into the braid, the raw material fiber mass and volume remain unchanged. This suggests that any tether using HMPE fiber material is strongly susceptible to VIV and drag increase.

However, the mass ratio m^* is not the only parameter determining the vibration amplitude A_y. The damping factor quantifies how much energy is shed off and dissipated per cycle relative to the total oscillation energy

$$\zeta = \frac{E_\mathrm{c} - E_{\mathrm{c}+1}}{4\pi E_\mathrm{c}}. \tag{2.30}$$

The oscillations of a string in a static fluid, such as in a pluck test, will decay over the oscillation cycles due to resistive surface pressures generated by the fluid during the oscillatory motion. According to Blevins [3], the natural logarithm of the amplitude ratio of any two successive cycles of a lightly damped structure in free decay equals to $2\pi\zeta$. For AWE applications, this would require making amplitude measurements or peak velocity measurements of a selected tether during a pluck test.

Assuming a logarithmic decrement of the oscillations, the product term $m^*\zeta$ is a non-dimensional parameter denoted as mass damping factor

$$\delta_\mathrm{r} = \frac{2\lambda(2\pi\zeta)}{\rho d^2}, \tag{2.31}$$

which is identical to the Scruton number Sc. The mass damping factor describes the effect of the tether diameter d on the oscillation amplitude A_y [3, 24].

The above considerations imply that the tensile structure is linear and viscously damped, suspended between fixed points. However, structural damping can also be due to absorption of energy by the flying wing, kite, winch and other connected system components. Consequently, it may prove difficult to use existing theory from literature alone to determine the oscillation characteristics.

2.4.6 Vibration Amplitude and Effect on Drag

Sarpkaya [24] has derived a simplified expression for the maximum oscillation amplitude A_y of a taut string or cable as a function of the mass damping factor δ_r

$$A_\mathrm{y} = \frac{0.369d}{\sqrt{0.06 + \left(2\pi \mathrm{St}^2 \delta_\mathrm{r}\right)^2}}. \tag{2.32}$$

From Blevins [3], Eq. (2.32) agrees well over the range $2 \times 10^2 < Re < 2 \times 10^5$. Understanding that other formulations of the maximum amplitude are proposed in

this reference, they are considered to be within 15% of each other. Further, when the mass damping term is greater than 64, the peak amplitudes are normally less than $0.01d$.

It is well known that larger oscillation amplitudes result in a larger effective aerodynamic drag $C_{\mathrm{D,eff}}$. For rigid cylinder experiencing transverse oscillations, a near linear fit exists from data compiled from multiple sources [24, 31, 33]

$$\frac{C_{\mathrm{D,eff}}}{C_{\mathrm{D}}} = 1 + 2.1\frac{A_{\mathrm{y}}}{d}, \tag{2.33}$$

where C_{D} is the cylinder drag at $A_{\mathrm{y}} = 0$.

It can be concluded that a string of lower mass in a higher density fluid shall experience larger oscillation amplitudes and thus drag coefficients well above nominal. Conversely, a string of higher mass in a lower density fluid is expected to experience lower amplitudes and drag coefficients closer to nominal. Pressure vectors associated with the small tether and large tether examples are illustrated in Fig. 2.8.

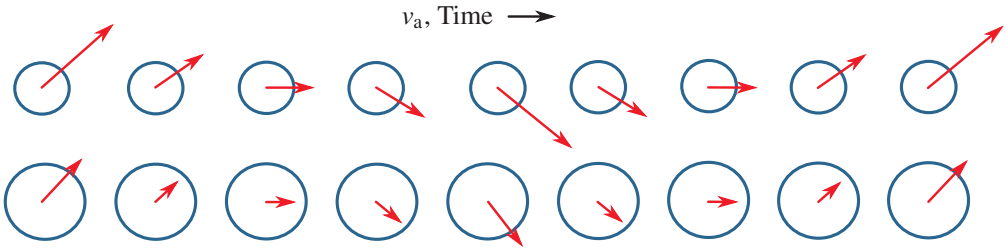

Fig. 2.8 Generic pressure vectors during one vortex shedding cycle of a string of lower mass in a higher density fluid (top), and one cycle of a string of higher mass in a lower density fluid (bottom)

The presented conventional framework of mass damping does not closely associate the magnitude of A_{y} to the natural frequency f_{n}. For the higher harmonic oscillations ($n = 2, 3, \ldots$) the tether body has less time to react to changes in the pressure vector direction and magnitude. The effect of shortened vortex shedding cycle times has been observed to reduce the oscillation amplitude and consequently the elevated drag associated with VIV [9].

For AWE applications, further analysis and likely testing will be required to determine the trend in VIV sensitivity due to mass damping as the diameter of tether increases and in the change of vibration amplitude A_{y} as the natural frequency f_{n} increases.

2.5 Elevated Drag Regimes

Vortex-Induced Vibrations (VIV) lock-in and galloping are two different aero-elastic coupling phenomena which can occur in AWE applications and which can substan-

tially affect the aerodynamic drag of the tensile structure connecting the aerodynamic lifting device with the ground. Because increased drag leads to reduced flight speeds the occurrence of these phenomena can negatively impact the performance of the AWE system. This section further details the aero-elastic mechanisms and maps the relevant regimes on the basis of wind tunnel measurements of Dunker [9].

2.5.1 Vortex-Induced Vibrations and Lock-in

Vortex-Induced Vibrations (VIV) are caused by unsteady flow separation from an elastic structure and the resulting cyclic variation of fluid forces. In reaction to these, the structure deforms, changing its kinetic and potential energy. The deformation motion in turn changes the relative flow with corresponding changes in the fluid forces. This fluid-structure coupling mechanism exhibits all physical contributions that are required for forced oscillations: an exciting periodic force, an elastic restoring force and inertia as well as aerodynamic damping.

The main implication for AWE is the case when the flow shedding frequency is in harmonic resonance with a natural frequency f_n of the tether and bridle line system. This type of resonance produces vibration amplitudes and aerodynamic drag many times larger than sub- and super-harmonic resonance where the vibration of the structure is at a specific multiple or fraction of the shedding frequency, respectively.

In basic physical terms, lock-in is the alignment of vortex shedding frequencies with the natural frequency of the vibrating structure. The alignment can be up- or down-shifted from the shedding frequency of the stationary structure to match the natural frequency over a range of freestream velocities. Since vortices are commonly formed at maximum displacement of a transverse vibration, the vibration frequency exerts some influence over vortex wake position as well as its phasing. A common range provided in literature as prone to lock-in is when $0.7 f_\mathrm{s} > f_\mathrm{n} > 1.3 f_\mathrm{s}$. During lock-in, the effective drag $C_{\mathrm{D,eff}}$ remains elevated over a range of velocities. Across this range, the tether or bridle line experiences a near constant vibration at the nearest natural frequency.

Vortex shedding produces cyclic drag and lift force components that act on the tensile structure, as shown in Fig. 2.4. As consequence of the vibrations, the shedding along the axis of the structure becomes more correlated [32] organizing the wake in three dimensions, the vortices become stronger [13], the drag increases [2] and in the case of traverse vibration, the ability of the shedding frequency to lock-in to the vibration frequency is increased [13]. For certain conditions, the propensity for a given vibration to create stronger vortices, to in turn create stronger amplitude vibrations and so on, can be seen. For a stationary structure with cylindrical cross section, lock-in can occur with as much as $\pm$ 40% deviation from the nominal shedding frequency.

A more detailed analysis of the physical phenomena governing lock-in, including the necessary illustrations to effectively communicate the vortex street formation

and phase, as well as the more complex principles of hysteresis and sub- and superharmonics, can be further sought in Blevins [3] and Naudascher [21].

Dunker [9] studied the lock-in characteristics of braided lines on the basis of wind tunnel measurements. As illustrated in Fig. 2.9, a line with $d = 1.5$ mm is seen to have a dominant vibration frequency matching a Strouhal number of $\mathrm{St} = 0.172$. For

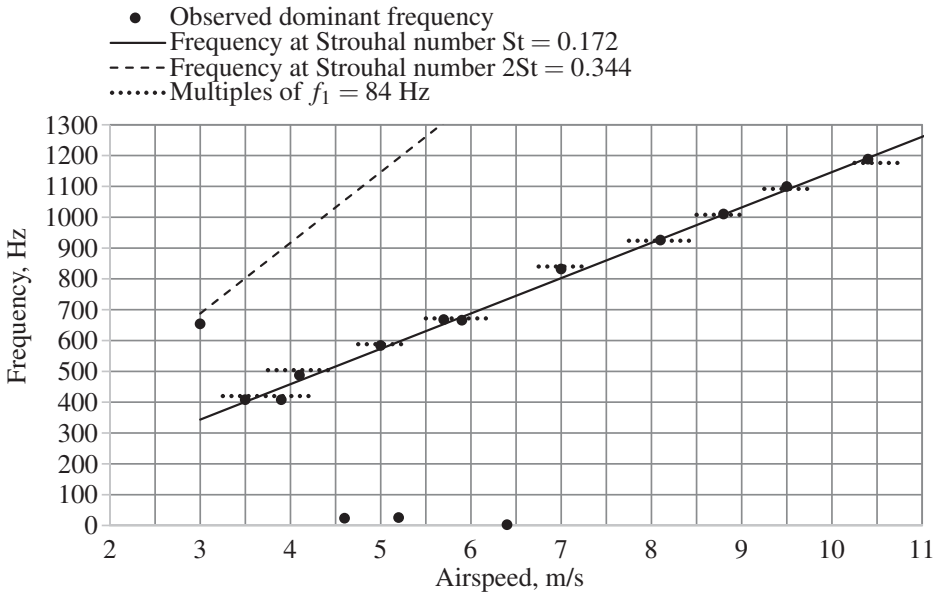

Fig. 2.9 Dominant vibration frequencies and lock-in for Dyneema® line with $d = 1.5$ mm and $\alpha = 76.5^\circ$ at $\mathrm{Re} = 300$ to 1000. Adapted from Dunker [9]

instances where a single lock-in was documented across a velocity range, one each vibration condition was observed on either side of the stationary shedding frequency Strouhal curve. The lock-in ranges occurring at 408 and 665 Hz are examples of this. The fundamental frequency for this line was obtained from a pluck test and was observed to be $f_1 = 84$ Hz.

Here it can be seen that the dominant frequency observed at the lowest measurement is at twice the shedding frequency. This is unusual in that the tether angle of attack is relatively small for this characteristic to occur, where normally this can occur for $\alpha < 60^\circ$.

Several instances of a major secondary vibration frequency were observed at twice the shedding frequency, however, these were not always the dominant vibration frequency. As mentioned previously, the lift force oscillations occur at the Strouhal frequency, but drag force oscillations can occur at twice the Strouhal shedding frequency. The vibration spectrum map in Fig. 2.10 displays both vibration modes. The magnitude of the peaks represents the relative dominance of the vibration frequency.

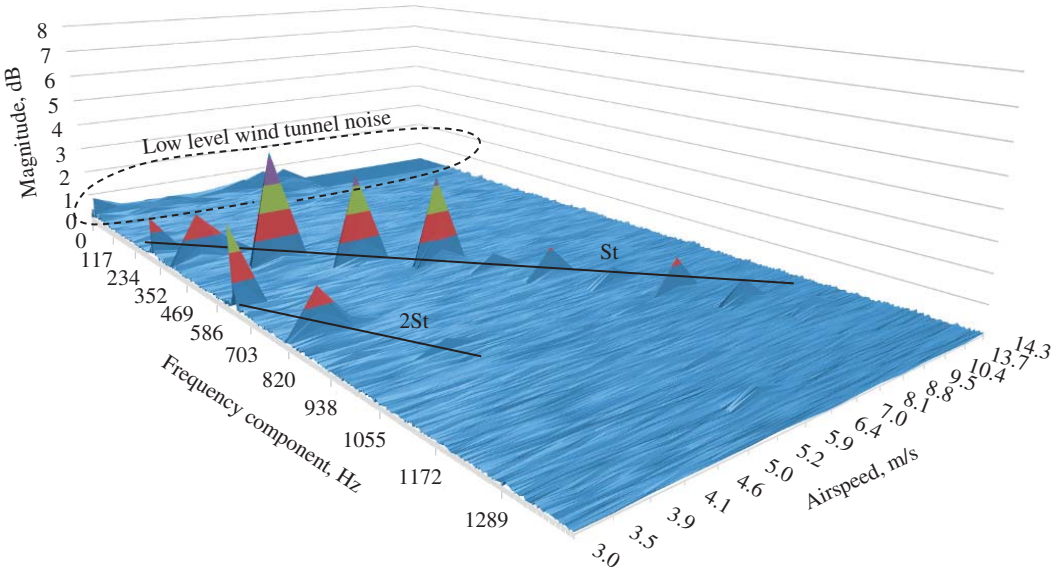

Fig. 2.10 Vibration spectrum map for a Dyneema® line with $d = 1.5$ mm at $\alpha = 76.5°$. Adapted from Dunker [9]

2.5.2 Impact on Aerodynamic Drag Characteristics

Because the vibration amplitude is maximum during lock-in, the resonance phenomenon negatively impacts the aerodynamic drag characteristics of the tether and bridle line system. Continuing with the example of a line with $d = 1.5$ mm, Fig. 2.11 compares the measured effect of lock-in on the line drag with the theoretical drag

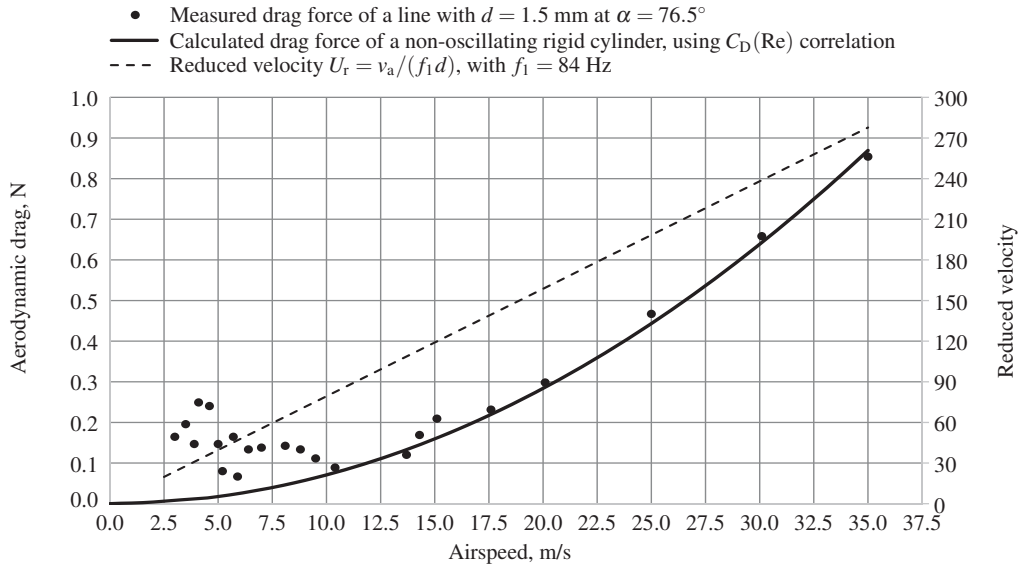

Fig. 2.11 Measured aerodynamic drag force and theoretical drag force of a rigid, non-vibrating cylinder. For the definition of the reduced velocity see Eq. (2.34). Adapted from Dunker [9]

of a rigid, non-vibrating cylinder. The most important observation is that several drag measurements exceed the theoretical baseline value by more than 300%. These instances of elevated drag mostly, but not exclusively, occur during observations of vibration and/or audible harmonics for the stated condition.

Here it is seen that higher velocities, those with expected smaller vibration amplitudes, match closer to the theoretical C_D-curve than lower velocities, even though the Strouhal frequency vibration mode is present. This closer correlation begins around airspeed 17.5 or 20 m/s, which is around the natural frequency f_{23}.

2.5.3 Galloping

Galloping is a movement-induced excitation of elastic tensile structures with non-circular cross sections which can result in very large amplitude vibrations at much lower frequencies than the shedding frequency. It is an aero-elastic phenomenon in which aerodynamic forces cause a distortion of the position or orientation of the structure. When the structure vibrates in a transverse uniform fluid flow its orientation with respect to the relative fluid flow is constantly changing, as depicted in Fig. 2.3. Consequently, the lift and drag components of the fluid force vary as the velocity of the structure under vibration varies. Above the critical freestream velocity of the structure, the result is a condition in which energy is fed into the vibration motion.

This is important for AWE applications as many tethers are braided, flexible and subject to distortion from braid style, repetitive winding and other handling operations and a tether with circular cross section can develop a non-circular cross section. A tether or line may also have a non-circular cross section upon manufacture. In power cables with twisted strand design, ice buildup of just 10% of the diameter is sufficient to produce plunge galloping [29].

Galloping generally comes in two forms, plunge galloping and torsional galloping, where the former is a transverse motion with one degree of freedom relative to the free stream flow v_a, as shown in Fig. 2.8, and the latter is a torsion motion along the structure axis, denoted as twist, as shown in Fig. 2.3. Mixed plunging modes are possible and involve inertial coupling, while the one degree of freedom models assume no inertial coupling [3]. Generally, the flow velocity v_a must be much higher than the vibration velocity $v_{t,\omega}$ of the structure, such that the fluid flow has time to react to the structural motion and to account for the varying vibration-induced angle of attack α_ω (see Fig. 2.3) or the angle of incidence ψ (see Fig. 2.2). For this reason, quasi-steady fluid dynamics can be assumed, which means that fluid forces are calculated using the instantaneous relative velocity and orientation of the structure.

Plunge galloping is sensitive to the aerodynamic characteristics of the tether of bridle line. For galloping to occur, a negative C_L at positive α_ω is required and vice versa [3]. Generally, plunge galloping is possible for cases where $f_s \gg f_1$, for a reduced velocity [3]

$$U_\mathrm{r} = \frac{v_\mathrm{a}}{f_1 d} > 20. \tag{2.34}$$

This non-dimensional parameter quantifies the distance covered by the mean flow during a single vibration cycle, measured in terms of the diameter, which is the characteristic length of the flow problem. Almost all AWE systems will nominally operate at $U_\mathrm{r} > 20$, which is also a condition underlying the measurements described in Fig. 2.11.

One example of plunge galloping, or potentially also combined plunge and torsional galloping, of a tensioned line at Reynolds numbers relevant for AWE is available from Siefers [28]. The investigated braided line of rectangular cross section with rounded corners, effective diameter of $d = 1.8$ mm and airspeed $v_\mathrm{a} = 27.5$ m/s experienced a vibration frequency of $f = 35.4$ Hz with an amplitude of about $A_\mathrm{y} = 5d$. The Strouhal frequency under the same conditions is approximately $f_\mathrm{s} = 2250$ Hz. The aspect ratio of the cross section of between $e/d = 2$ to 3 is consistent with the predictions of Naudascher [21] which indicate a possible galloping range of $e/d = 1$ to 3.

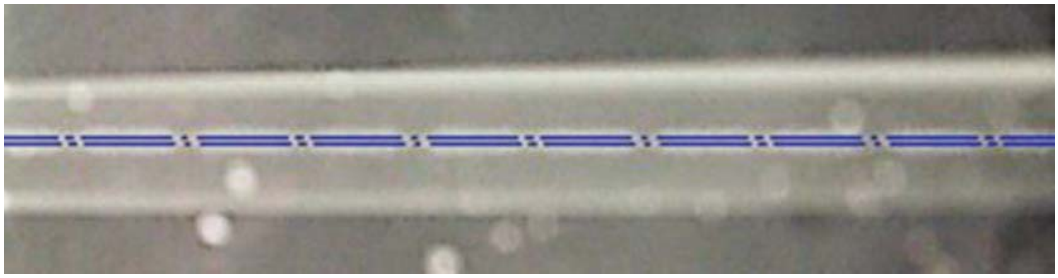

Fig. 2.12 Tensioned line with rectangular cross section and rounded corners experiencing plunge galloping in wind tunnel tests [28]. Stationary line indicated by blue lines, up/down vibration of the line in this photo is at an amplitude of about $A_\mathrm{y} = 4d$ at a reduced velocity $U_\mathrm{r} = 441$

The tests presented by Siefers [27] indicate only minimal increases of aerodynamic drag by plunge galloping. While it is important to note that very large amplitude oscillations are possible under plunge galloping, e.g. power lines have experienced amplitudes as high as 10 m [21], this may not impact the drag values substantially. However, although system level interactions are not discussed in this chapter, such amplitudes would provide a potential inertial-based forcing function from the tether into the flying apparatus which would need to be considered when a system level analysis is performed.

In torsional galloping, the tether is reoriented about its axis in the relative flow with velocity v_a via the twist angle of incidence ψ and the corresponding angular velocity $\dot{\psi}$ [23]. Torsional galloping leads to varying angles of attack along the entire length of the structure. The phenomenon is sensitive to the torsional spring constant k, a material-structure property resisting twist deformation, and the aerodynamic moment coefficient C_M.

Blevins [3] provides a torque galloping onset parameter, but as it is not based on a threshold value as in plunge galloping, rather instead on a number of parameters de-

pendent on cross section shape other than circular, a guideline for AWE applications cannot be extracted. Torsional galloping will need to be evaluated on a case-by-case basis for tethers or bridle lines with non-circular cross sections.

Tethers or bridle lines with cross section aspect ratios of $e/d > 1$ can have cross sectional aerodynamic characteristics C_D, C_L and C_M which vary significantly with the twist angle ψ and should thus be considered strongly susceptible to torsion galloping. For torsional galloping to occur generally a negative moment coefficient C_M at positive ψ is required and vice versa [3].

Siefers [27] also observed torsional galloping with C_D up to 210% larger than the average static result. It is noted that with torsional galloping an increase in surface area is exposed to the freestream flow, which could potentially contribute to the changes in drag force, however, torsional amplitude resulted in ψ less than 19° for this testing.

The prediction of galloping for tethers and bridle lines is dependent on knowing the coefficients of lift, drag and moment for various angles of incidence ψ with respect to the relative flow, and the torsional spring constant, which will all be unique for each tether or line. The potential for galloping and elevated drag forces is present, however this result will remain unique to each tether or line.

Tethers, while not perfectly cylindrical, are normally axis-symmetric, of general round cross section and have cross section aspect ratios of around $e/d = 1$ and are thus not strongly prone to galloping, especially torsional galloping. However, as mentioned, caution should be taken when any deformation from this round cross section does occur, e.g. during manufacturing or from processes such as winding or other handling. Full scale testing of tethers should be attentive to vibration modes observed.

2.5.4 Evaluation of Tether Usages

AWE systems with a static tether that predominantly operates in a fixed location, such as for buoyant lifting devices, are generally exposed to more uniform freestream velocities than dynamic tether systems. Additionally, much lower airspeeds are expected since the tether is not moving. This results in a lower reduced velocity, as defined in Eq. (2.34), but still with a value $U_\mathrm{r} > 20$, which is the general threshold for galloping to occur. For static tether systems both lock-in vibration and galloping modes can thus occur.

AWE systems with a tether that pivots about a fixed ground location, are subject to varying local conditions of airspeed, Reynolds number and angle of incidence as functions of the radial distance from the ground. The basic kinematics are illustrated in Fig. 2.1. Although not in all situations, such as in downwind flight, the relative velocity generally increases as a function of the radial distance along the tether. This affects the local shedding frequency along the tether or bridle line, which likewise increases with tether length.

Assuming that vibration lock-in is possible within the vortex shedding regime $0.7f_s < f_n < 1.3f_s$, the susceptible regions of a tether can be determined. Potentially many different localized lock-in regions could coexist along the tether. These regions would be separated by regions of tether that are not locked-in. An example of a tether with multiple lock-in regions is shown in Fig. 2.13. It is yet uncertain how multiple lock-in regions and corresponding dormant regions would interact and whether multiple localized modes could be achieved in one contiguous tether.

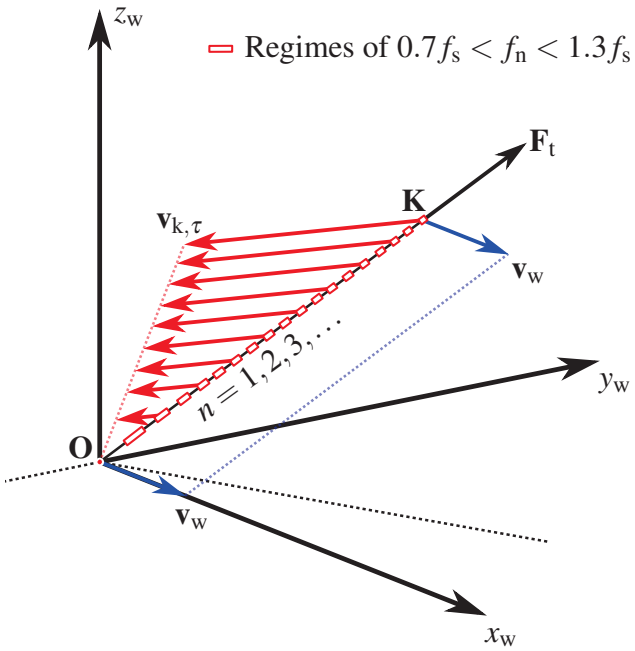

Fig. 2.13 Tether with lock-in regions determined on the basis of the local relative flow velocity at the tether. Compare also with Fig. 2.1 for more kinematic details. The tether regions outlined in red beyond this first region would increment by 1 and would dependent on wind velocity and local tether velocity. The lock-in regions become narrower with increasing distance from the ground attachment point

Both VIV and galloping are conventionally analyzed at a constant freestream velocity v_a. It can be assumed that the constantly changing relative flow conditions of dynamic tether systems impede the formation and sustainment of steady galloping cycles. Vortex shedding, however, will always occur. When vortex-induced vibrations are possible and lock-in conditions are met, the lock-in can occur much quicker than a gallop, appearing instantaneously. A challenge for AWE will be to understand the reaction of vortex forces that occur at fundamentally different frequencies along a line.

Audible tones or whistling of a tether in flight are generally strong indicators for vibration lock-in. While the induced vibrations substantially increase the aerodynamic drag, attention should also be given to eliminate the audible tones that emanate from tethers and bridle lines that are not obviously vibrating, i.e. Strouhal frequency tones. The literature on the topic is insufficient to determine whether elimination of sound has an impact on drag as a result of advantageously controlling the shedding frequency.

The need to investigate multiple vibration regimes in a single tether is a valid concern. Multiple vibration modes have at least occurred in subspan galloping, where,

by definition, a localized subsection of a cable oscillates at a different frequency and amplitude than other sections of the same cable.

2.6 Mechanisms to Attenuate Vibration and Reduce Drag

Mechanisms to reduce aerodynamic drag are based mostly on the attenuation of vibration phenomena. A number of additive design concepts exist to reduce VIV for tensile structures with cylindrical cross section. These comprise helical strakes, shrouds, slats, fairings, splitters, ribbons, guide vanes and spoiler plates.

Blevins [3] provides illustrated examples and further references of these concepts. The challenge for AWE applications is to incorporate these into a flexible, elastic, braided textile that is typically wound onto a large drum under tension. Any concept that considers tethers or bridle lines with other than round cross section will need a serious solution to maintaining desired orientation or risk elevated nominal drag, galloping, tether controllability, winding ability onto a spool and more.

Although thicker in cross section, a kite boarding line with helical strake braiding yielded a lower drag over some velocities of interest than a thinner line with round cross section [9]. Examples are shown in Fig. 2.14. The strake disrupts synchro-

Fig. 2.14 Examples of helical strake braiding of kite boarding lines

nization of trailing vortices and modulates the local Strouhal number [22]. The drag force improvement was attributed to the reduced susceptibility to VIV. Although some vibration effects were still observable, the concept can potentially be used for AWE applications. Further development and understanding of the relevant vibration regimes in laboratory and full scale environments are required.

Another option is the addition of an aerodynamically shaped fairing to the tether [1, 14]. These concepts promise not only better flow control and less susceptibility to all forms of vibration-induced drag, but also consistently reduce the drag across a wide range of scales and airspeeds.

Jung [16] has shown that the addition of latex coating to a variety of fast rope braids for helicopters consistently reduced the drag coefficient by 15 to 50%, depending on size and braid construction. Several of the analyzed ropes are in the diameter range of large-scale AWE applications. However, braiding styles were gen-

erally much rougher and fuzzier, using different materials than common for AWE. Given the tested range of braid geometries, the direct carry-over of this technique to AWE applications is uncertain.

Laboratory experiments of selective air ejection along the cylinder axis have shown to decrease drag coefficients by approximately 20% [17]. Although a round cross section could be maintained on the basis of this concept, the complexity of the air duct and ejection system seems prohibitive for AWE applications.

2.7 Conclusion

This chapter has introduced the physics of tether and bridle line drag in airborne wind energy (AWE) applications. It has further provided a compilation of experimental data and correlations to analyze line drag and identify regimes of elevated drag caused by Vortex-Induced Vibration (VIV) and by galloping. AWE developers and researchers should find relevant ranges of Reynolds numbers, drag and friction coefficients, Strouhal numbers and natural frequencies or the information necessary to retrace these in the given literature sources.

Correlations for predicting the vibration amplitude and the corresponding effective drag coefficients are presented in the application context of AWE. Further references have been provided to supplement finer details and complexities beyond the scope of this introductory chapter. Lock-in and galloping phenomena were shown in laboratory experiments to have elevated drag regimes, where drag forces were observed to be over 300% for lock-in and up to 210% for torsional galloping.

Both lock-in and galloping have been shown to be relevant vibration modes for static tether systems but only lock-in as being potentially relevant for dynamic tether systems. Dynamic tether systems will experience shedding frequencies sufficient to align with a natural frequency of the tensile structure and to achieve lock-in. However, because of the constantly varying airspeed along the tensile structure operated in crosswind motion, the vibration response to multiple lock-in frequencies that occur along the tensile structure is not yet certain and subject to future research. Finally, a collection of conventional and more recent VIV suppression solutions were presented which could be utilized by AWE applications.

References

1. Bevirt, J.: Tether Sheaths and Aerodynamic Tether Assemblies. US Patent 0,266,395, 2011
2. Bishop, R. E. D., Hassan, A. Y.: The Lift and Drag Forces on a Circular Cylinder in a Flowing Fluid. Proceedings of the Royal Society of London A: Mathematical, Physical and Engineering Sciences **277**(1368), 51–57 (1964). doi: 10.1098/rspa.1964.0005
3. Blevins, R. D.: Flow Induced Vibration. 2nd ed. Krieger Publishing Company, Malabar, FL, USA (2001)

4. Bootle, W. J.: Forces on an inclined circular cylinder in supercritical flow. AIAA Journal **9**(3), 514–516 (1971). doi: 10.2514/3.6213
5. Bosman, R., Reid, V., Vlasblom, M., Smeets, P.: Airborne Wind Energy Tethers with High-Modulus Polyethylene Fibers. In: Ahrens, U., Diehl, M., Schmehl, R. (eds.) Airborne Wind Energy, Green Energy and Technology, Chap. 33, pp. 563–585. Springer, Berlin Heidelberg (2013). doi: 10.1007/978-3-642-39965-7_33
6. Breukels, J.: An Engineering Methodology for Kite Design. Ph.D. Thesis, Delft University of Technology, 2011. http://resolver.tudelft.nl/uuid:cdece38a-1f13-47cc-b277-ed64fdda7cdf
7. Cherubini, A., Papini, A., Vertechy, R., Fontana, M.: Airborne Wind Energy Systems: A review of the technologies. Renewable and Sustainable Energy Reviews **51**, 1461–1476 (2015). doi: 10.1016/j.rser.2015.07.053
8. Drescher, H.: Messung der auf querangeströmte Zylinder ausgeübten zeitlich veränderten Drücke. Zeitschrift für Flugwissenschaften und Weltraumforschung **4**, 17–21 (1956)
9. Dunker, S.: Experiments in Line Vibration and Associated Drag for Kites. AIAA Paper 2015-2154. In: Proceedings of the 23rd AIAA Aerodynamic Decelerator Systems Technology Conference, Daytona Beach, FL, USA, 30 Mar–2 Apr 2015. doi: 10.2514/6.2015-2154
10. Dunker, S.: Ram-Air Wing Design Considerations for Airborne Wind Energy. In: Ahrens, U., Diehl, M., Schmehl, R. (eds.) Airborne Wind Energy, Green Energy and Technology, Chap. 31, pp. 517–546. Springer, Berlin Heidelberg (2013). doi: 10.1007/978-3-642-39965-7_31
11. Fage, A., Warsap, J. H.: Effects of turbulence and surface roughness on drag of circular cylinders. Reports and memoranda 1283, Aeronautical Research Committee, Oct 1929. http://naca.central.cranfield.ac.uk/reports/arc/rm/1283.pdf
12. Goldstein, L.: Airborne wind energy conversion systems with ultra high speed mechanical power transfer. In: Ahrens, U., Diehl, M., Schmehl, R. (eds.) Airborne Wind Energy, Green Energy and Technology, Chap. 13, pp. 235–247. Springer, Berlin Heidelberg (2013). doi: 10.1007/978-3-642-39965-7_13
13. Griffin, O. M., Ramberg, S. E.: On vortex strength and drag in bluff-body wakes. Journal of Fluid Mechanics **69**(04), 721 (1975). doi: 10.1017/S0022112075001656
14. Griffith, S., Lynn, P., Montague, D., Hardham, C.: Faired tether for wind power generation systems. Patent WO 2009/142762, 26 Nov 2009
15. Hoerner, S. F.: Fluid-Dynamic Drag. Bricktown, Brick Town, NJ, USA (1965)
16. Jung, T. P.: Wind Tunnel Study of Drag of Various Rope Designs. AIAA Paper 2009-3608. In: Proceedings of the 27th AIAA Applied Aerodynamics Conference, San Antonio, TX, USA, 22–25 June 2009. doi: 10.2514/6.2009-3608
17. Kim, J., Choi, H.: Distributed forcing of flow over a circular cylinder. Physics of Fluids **17**, 033103 (2005). doi: 10.1063/1.1850151
18. King, R.: A review of vortex shedding research and its application. Ocean Engineering **4**(3), 141–171 (1977). doi: 10.1016/0029-8018(77)90002-6
19. Lienhard, J. H.: Synopsis of lift, drag, and vortex frequency data for rigid circular cylinders. Research Division Bulletin 300, Washington State University, Pullmann, WA, USA, 1966. http://www.uh.edu/engines/vortexcylinders.pdf
20. Loyd, M. L.: Crosswind kite power. Journal of Energy **4**(3), 106–111 (1980). doi: 10.2514/3.48021
21. Naudascher, E., Rockwell, D.: Flow-Induced Vibrations: An Engineering Guide, Chap. 2–3, 7, 9. A. A. Balkema Publishers, Rotterdam, The Netherlands (1994)
22. Nebres, J. V., Batill, S. M.: Flow around a cylinder with a spanwise large-scale surface perturbation. AIAA Paper 93-0657. In: Proceedings of the 31st Aerospace Sciences Meeting, Reno, NV, USA, 11–14 Jan 1993. doi: 10.2514/6.1993-657
23. Oudheusden, B. W. van: Investigations of an aeroelastic oscillator: Analysis of one-degree-of-freedom galloping with combined translational and torsional effects. LR-707, Delft University of Technology, Dec 1992. http://resolver.tudelft.nl/uuid:0d3c0eac-2bab-422a-9e0f-8c74da19dcd0

24. Sarpkaya, T.: Fluid Forces on Oscillating Cylinders. Journal of the Waterway, Port, Coastal and Ocean Division **104**, 275–290 (1978)
25. Schlichting, H.: Boundary-layer theory. McGraw-Hill (1979)
26. Schmehl, R. (ed.): Book of Abstracts of the International Airborne Wind Energy Conference 2015. Delft University of Technology, Delft, The Netherlands (2015). doi: 10.4233/uuid:7df59b79-2c6b-4e30-bd58-8454f493bb09
27. Siefers, T. M., Campbell, J. P., Clark, D. K., McLaughlin, T. E., Bergeron, K.: Quantification of Drag from Flat Suspension Line for Parachutes and the Influence of Flow Induced Vibrations. AIAA Paper 2016-1777. In: Proceedings of the 54th AIAA Aerospace Sciences Meeting, San Diego, CA, USA, 4–8 Jan 2016. doi: 10.2514/6.2016-1777
28. Siefers, T., Greene, K., McLaughlin, T., Bergeron, K.: Wind and Water Tunnel Measurements of Parachute Suspension Line. AIAA Paper 2013-0064. In: Proceedings of 51st AIAA Aerospace Sciences Meeting, Grapevine (Dallas/Ft. Worth Region), TX, USA, 7–10 Jan 2013. doi: 10.2514/6.2013-64
29. Simpson, A.: Fluid-Dyamic Stability Aspects of Cables. In: Shaw, T. L. (ed.) Mechanics of Wave-Induced Forces on Cylinders, pp. 90–132. Pitman Publishing Ltd., London (1979)
30. Strouhal, V.: Ueber eine besondere Art der Tonerregung. Annalen der Physik und Chemie **5**(10), 216–251 (1878). http://www.deutschestextarchiv.de/strouhal_tonerregung_1878
31. Tanida, Y., Okajima, A., Watanabe, Y.: Stability of a circular cylinder oscillating in uniform flow or in a wake. Journal of Fluid Mechanics **61**(4), 769–784 (1973). doi: 10.1017/s0022112073000935
32. Toebes, G. H.: The Unsteady Flow and Wake Near an Oscillating Cylinder. ASME Journal of Basic Engineering **91**(3), 493–502 (1969). doi: 10.1115/1.3571165
33. Tørum, A., Anand, N. M.: Free Span Vibrations of Submarine Pipelines in Steady Flows-Effect of Free-Stream Turbulence on Mean Drag Coefficients. Journal of Energy Resources Technology **107**(4), 415–420 (1985). doi: 10.1115/1.3231212
34. Vlugt, R. van der, Peschel, J., Schmehl, R.: Design and Experimental Characterization of a Pumping Kite Power System. In: Ahrens, U., Diehl, M., Schmehl, R. (eds.) Airborne Wind Energy, Green Energy and Technology, Chap. 23, pp. 403–425. Springer, Berlin Heidelberg (2013). doi: 10.1007/978-3-642-39965-7_23